

Experimental evaluation of swelling and induced embedment by CO₂ in the propped artificial fracture in shale

Lei Hou ^a, Derek Elsworth ^b, Xueyu Geng ^a

^a School of Engineering, The University of Warwick, Coventry CV4 7AL, UK

^b Energy and Mineral Engineering, EMS Energy Institute and G3 Center, Pennsylvania State University, University Park, 16802, USA

Abstract

Swelling and embedment exert significant influence on the evolution of permeability in propped fractures, potentially consuming half the original gain in permeability. We measure the evolution of permeability in propped fractures of shale to both adsorbing CO₂ and non-adsorbing He – accommodating the impacts of aperture change due to proppant pack compaction, particle deformation, and reversible and irreversible embedment. A typical linear relation is obtained in He cases as well as U-shaped curve for gaseous CO₂ and W-shaped curve for supercritical CO₂, which are proven to be dominated by the effective aperture and particle interval. An exception is discovered for liquid CO₂, where the high injection pressure contributes as much as the swelling does and results in a linear curve with the lowest permeability. Concretely, approximately 50 ~ 70 % of the permeability recovers from the recovery of swelling after the desorption of CO₂. The swelling, by itself, contributes 5 to 35 % of the total aperture reduction according to the adsorped mass. It also aggravates the embedment by 1.3 to 1.7 times before and after an injection of CO₂. A new calibration equation of swelling and induced embedment has been generated by bringing in the Langmuir isothermal equation and verified with former experiments with different rock and sorbing gas types. Stability and accuracy of the predictions demonstrate the universality of the new method that will benefit both enhanced gas recovery and CO₂ segregation

Keywords: swelling, embedment, propped shale fracture, permeability, carbon dioxide

1 Introduction

CO₂ as a solvent and waste product in the energy industries has a long history including for EOR (Enhanced Oil Recovery)(Alvarado & Manrique, 2010), CO₂ fracturing (H. Liu, Wang, Zhang, Meng, & Duan, 2014; Middleton et al., 2015; X. Zhang, Lu, Tang, Zhou, & Liao, 2017) and for storage in saline aquifers and depleted reservoir (Bielicki et al., 2018; Goodman et al., 2019; Rani, Padmanabhan, & Prusty, 2019). As a strong adsorptive gas, the permeability evolution involving CO₂ is one of the essential issues. The sorbing CO₂ swells the rock matrix and causes a reduction in the natural fracture aperture (H.-H. Liu & Rutqvist, 2009; Mazumder & Wolf, 2008; Pini, Ottiger, Burlini, Storti, & Mazzotti, 2009). This swelling behaviour follows the Langmuir Isotherm and usually approaches the maximum influence at twice of the Langmuir pressure (S. Wang, Elsworth, & Liu, 2011). The competition between swelling and effective stress results in a typical U-shaped curve for both integrated and split sample (Kumar, Elsworth, Liu, Pone, & Mathews, 2015; S. Wang, Elsworth, & Liu, 2013). Recently, a W-shaped curve has been discovered for the supercritical CO₂ case (Zhi, Elsworth, & Liu, 2019).

An accompanying issue with a similar significant impact on permeability is the particle embedment in propped fractures, which happens when the particle has higher stiffness than the rock. The embedment, by itself, will induce 10 to 60 % reduction in fracture aperture with subsequent 78.05 % conductivity loss in shale (Bandara et al., 2019; Santos et al., 2018; Jingchen Zhang & Hou, 2016). Former researches have taken the mineral composition (clay content), rock mechanics, interaction between rock surface and fracturing fluid, closure stress, proppant concentration and formation temperature and pressure, et al., into consideration (Arshadi et al., 2017; Tang & Ranjith, 2018; Wen et al., 2007; Junjing Zhang et al., 2015). Yet, the swelling is less concerned especially for the shale with lower organic content and higher stiffness. Besides, the conventional methodologies applied in those former studies are incompetent for the distinction of swelling and embedment with either a static loading or an API (American Petroleum Institute) standard conductivity test. Associated with swelling, the embedment develops more severely for the lower Young's Modulus reduced by the sorbing gas. A recent experiment in propped shale has demonstrated the significant effect of swelling

on permeability evolution, which also results in a typical U-shaped curve as shown in the coal sample (Li et al., 2017).

Nonetheless, the behaviour of swelling and induced embedment and their respective contribution to the permeability consumption are still not well known because the direct observation of swelling can hardly be realized in real-time under triaxial pressurized, sealed and gas injected conditions.

Therefore, we explore the swelling induced embedment of proppant in artificial fluid-driven fractures. We measure permeability loss with the injection of both non-adsorptive Helium (He) and adsorptive carbon dioxide (CO₂) on samples of Green River shale to (i) quantitatively reveal the the respective roles of swelling and embedment, (ii) define the different controlling mechanisms of permeability evolution, and (iii) define a model for embedment that accommodates the influence of swelling that provides a better prediction of fracture conductivity and understandings of gas production and CO₂ segregation.

2 Methodology

We measure permeability evolution to CO₂ and He in propped fractures in both shale (that accommodate embedment and swelling) and granite (that excludes these effects) via pressure transient (pulse) methods. We build main parts of the apparatus (core holder and reservoirs) in a water tank that constitutes a thermostat for supercritical CO₂. Then, we measure the permeability with CO₂ and He alternatively in the same sample. Based on the outcomes, we define the controlling mechanisms of permeability evolution and a modified calculation for embedment.

2.1 Materials and preparation

Axially-split core samples (25mm diameter 50mm length) of Westerly granite and Green River shale are placed in a pressurized coreholder with proppant sandwiched in the fracture. The proppant comprises high strength Carbo-Lite ceramic particles separately in size fraction 40/80 mesh. A single layer of proppant is first sandwiched between the two facing artificial fractures. In particular, we explore the behaviour of a monolayers since the deformation of proppant can be calculated more accurately, has relatively less impact on the fracture aperture and leaves swelling and embedment as the main factors influencing the permeability evolution. The proportion of monolayer propped fractures in field fracturing is significant. This is apparent in branch fractures or micro-fractures and

composes a crucial amount of the total stimulated reservoir volume (Gale, Laubach, Olson, Eichhüble, & Fall, 2014; Hoek & Martin, 2014; Weng, 2015). We use sorbing CO₂, (purity of 99.995%) and essentially non-sorbing He (99.999%) as flowing permeants for the permeability measurement.

2.2 Apparatus

A standard triaxial apparatus, as shown in Fig. 1, is used as a pressurized core holder. The proppant sandwiched sample is packaged with tape then jacketed in a Viton rubber jacket to seal and isolate the sample from the confining fluid in the chamber. This is then placed in the triaxial core holder (Temco) where both confining and axial stresses to 25 MPa are applied by syringe pump (ISCO 500D) with control to ± 0.007 MPa. The axial stress is transmitted directly onto both ends of the sample through axial platens which connect flow lines to fluid distributors. The end-platens are connected to two stainless steel gas reservoirs through tubing and isolating valves at both upstream and downstream reservoir sample ends. Reservoir volumes are 26.7 ml for the upstream and 16.8 ml for the downstream with reservoir pressures measured by transducers (Omega PX302-2KGV and Omega PX302-5KGV) to resolutions of ± 0.03 MPa. Each transducer is calibrated for each new sample with National Instruments Labview used for data acquisition and pump control.

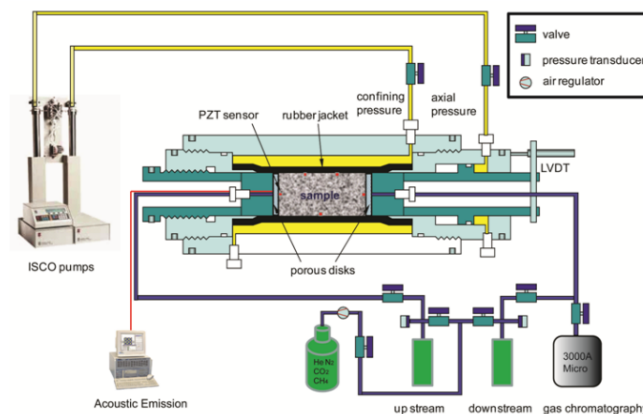


Fig. 1. Schematic of the experimental apparatus (S. Wang et al., 2011).

2.3 Procedure

We use standard pressure transient (pulse) methods for permeability measurements. Once the sample is in the core holder, the system is first evacuated for one hour and then saturated with the desired gas (CO₂ or He). Then, a pressure difference (pulse) is applied between upstream and downstream and its decay behaviour is recorded and analysed to obtain the permeability (S. Wang et al., 2011). The tests are performed at both room temperature (23 °C) and supercritical temperature (45 °C) in a water tank,

as shown in Fig. 2. The gas pressure falls in the range between 2 and 13 MPa to reach various phase states of CO₂.

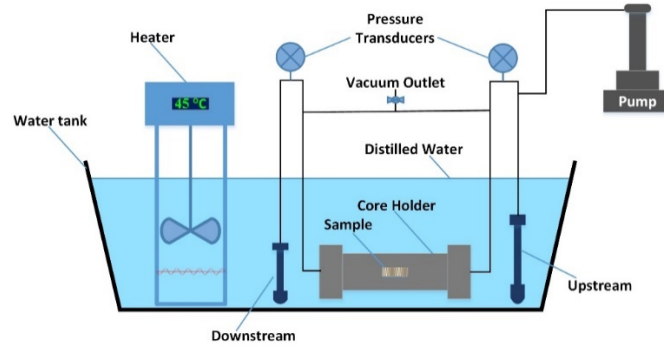


Fig. 2. Schematic of water tank heating system.

Particularly, we measure the alternative permeabilities with CO₂ and He in the same sample to evaluate the permeability recovery from the recovery of swelling. Then, a comprehensive analysis is performed for the quantitative description of swelling and embedment. As a part of the standard pulse decay method, the permeability is calculated by (Brace, Walsh, & Frangos, 1968)

$$k = \frac{\alpha\mu\beta LV_{up}V_{dn}}{A(V_{up} + V_{dn})} \quad (1)$$

Where α is the slope of pressure decay against time in a semi-log plot; μ and β are the viscosity and compressibility of the fluid, respectively; L is the length of the sample; V_{up} and V_{dn} are volumes of upstream and downstream reservoirs, respectively; A is the fluid flow cross-section area.

In this study, the contribution of sample bodies to permeability is ignored for the existing of the propped fracture. Thus, the cross-section area A is calculated by the average particle diameter timing the sample diameter. Besides, the compressibility of the fluid β is calculated from the bulk modulus

$$\beta = \frac{1}{B_M} = \frac{1}{v^2\rho} \quad (2)$$

Where B_M is the bulk modulus; v is the speed of sound in fluid; ρ is the fluid density.

The values of v and ρ are referred to the public data from the National Institute of Standards and Technology (NIST) in the US, as shown in Fig. 3. The density and speed of sound in He increase linearly with pressure in a relatively small range. Yet, those properties of CO₂ jump or fall sharply around the phase changing pressure.

The properties of CO₂ vary with pressure more continuously at 45 °C than those at 23 °C. Both of them decline at a higher temperature, especially under high pressure.

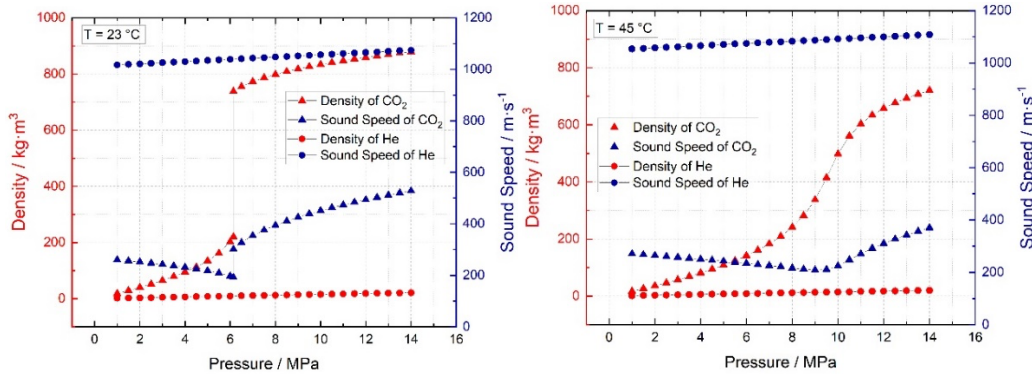


Fig. 3. Density and speed of sound in CO₂ and He (NIST database).

3 Results

A total of five groups of permeability measurements have been conducted with multiple repeats in each of these five groups with each probing injection (increasing gas pressure) and depletion (decreasing gas pressure) directions for at least three times. The measurements are for CO₂ as gaseous, liquid and supercritical fluid and He as gaseous. The permeabilities for the granite sample are used as a reference. Shale sample A was used for multi-purpose testing with repeat tests with He performed on samples B, C and D to measure the permeability recovery after CO₂ induced swelling and corresponding embedment. The experimental matrix is shown in Table 1.

Table 1. Matrix of experimental parameters.

Sample Type & No.	Westerly Granite	Greenriver Shale			
		A	B	C	D
Dimensional	25 * 50 mm				
Proppant	Carbo-Lite Ceramisite; 40/80 Mesh (D = 0.177 ~ 0.400 mm)				
Gas Type	Helium	Helium & Carbon Dioxide			
Confining & Axial Pressure	25 MPa				
Injection Pressure	3 ~ 9 MPa	3 ~ 13 MPa	2 ~ 9 MPa	2 ~ 13 MPa	2 ~ 10 MPa
Temperature	23 °C				45 °C

3.1 General testing results

The permeability evolution in granite and shale (sample) A are shown in Fig. 4. Generally, the granite has the largest permeability followed by the “shale + He” case, in which approximately half of the permeability is consumed by the embedment. The lowest permeability is obtained in the liquid CO₂ case. The positive linear relationships between gas pressure and permeability are found in those cases. The swelling and more serious corresponding embedment minish the permeability significantly in the gaseous CO₂ case. A typical U-shaped curve is formed because of the competition between adsorption

and effective stress. The curve reaches the bottom around double Langmuir pressure about 5MPa in this case. The dramatic drop around 7 MPa has been explained by the sudden volume change during the phase transition and the relatively stable pressure (Li et al., 2017). The gaseous and liquid CO₂ cases remain continuously in permeabilities around overlapped pressures (7 ~ 9 MPa).

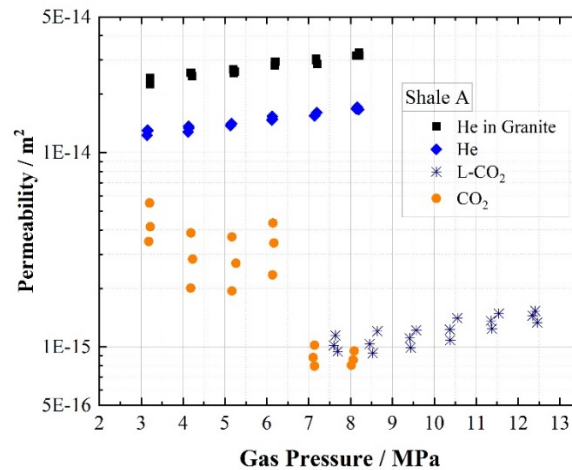


Fig. 4. Permeability evolution versus gas pressure in granite and shale sample A with injections of He, CO₂ (gaseous) and liquid CO₂ (L-CO₂). The temperature is 23 °C.

3.2 Permeability recovery behaviour

The repeating tests on shale sample B, C and D have revealed the permeability recovery behaviour by the recovery of swelling. The permeability returns to 50 ~ 70 % of the initial value in the repeating He test after injecting CO₂ and shows a parallel linear trend with the prior measurements, as shown in Fig. 5. It is worth noting that the recovery period is relatively short. The comparative trial has been conducted in different recovering periods(hours and days), and similar results have been received. Even though, we vacuumize the system for at least one hour to ensure the complete recovery of swelling.

Besides, the three groups of the experiments have presented relatively good repeatability in both values and trends. The minor difference in repeating He permeability has been found in sample D, where the operating temperature is 45 °C and CO₂ exists in the supercritical phase state. Nearly 70 % of the permeability restores, which rises by 20 % compared with the gaseous CO₂ cases. Moreover, a W-shaped curve has been found in the supercritical CO₂ case, which is in accordance with the discovery in integrated coal sample and has been explained by the synthetic effect of phase transition around the critical point and the plasticization of supercritical CO₂ (Zhi et al., 2019).

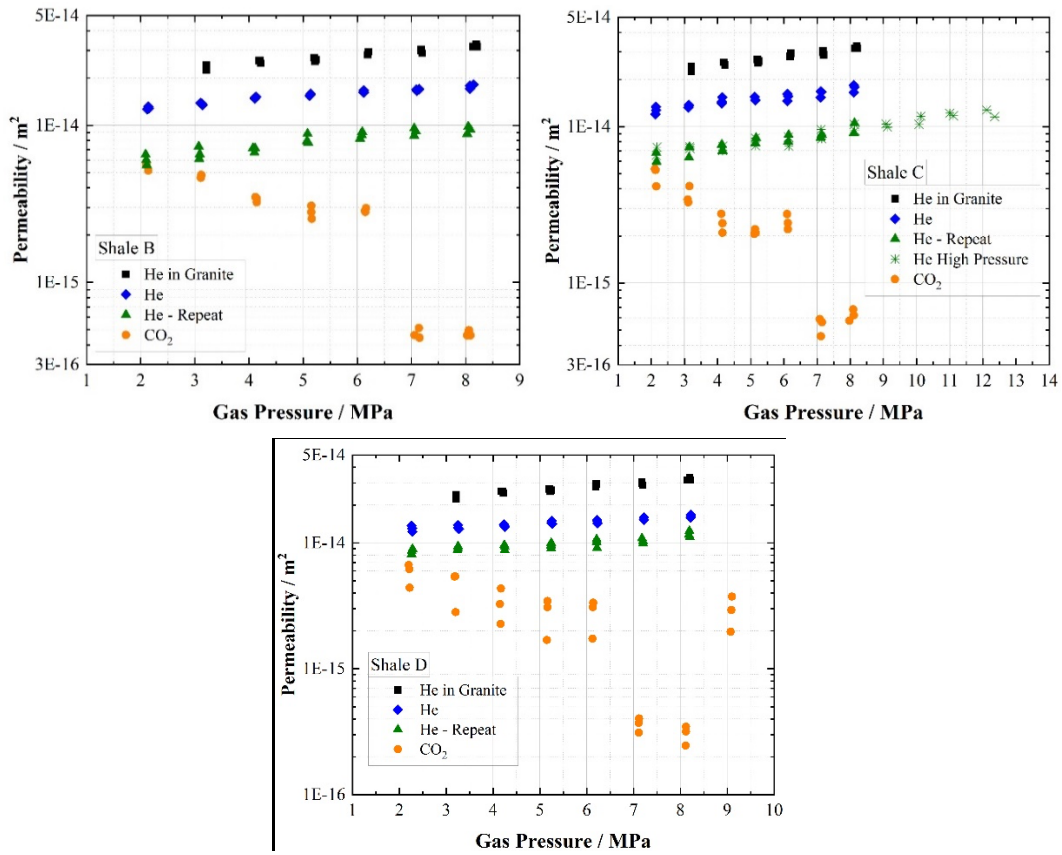


Fig. 5. Permeability evolutions in sample B, C and D. The experimental temperatures are 23 °C for sample B and C and 45 °C for sample D. The “He - Repeat” is the He permeability after injecting CO₂. The “He High Pressure” aims to verify the testing consistency under higher pressure condition.

4 Discussion

The swelling and embedment mechanisms can be visually explained by Fig. 6. Particularly, the particle deformation is considered as the third dominative aspects. The following assumptions are proposed and demonstrated in the latter analyses:

- (1) Particle deformation in the normal direction to the fracture surface (“c” in Fig. 6) is ignorable compared with the embedment;
- (2) Particle deformation in the parallel direction to the fracture surface (“a” in Fig. 6) is non-negligible within the non-sorbing gas cases in shale;
- (3) The deformation of the sample under triaxial pressure is negligible.

The original flowing space is similar to porous media and consists of gaps between particles shown in the detail view in Fig. 6. Each segment can be roughly described by the aperture (b) and particle interval (w) with initial values of b_0 and w_0 , respectively. After putting on confining pressure and injecting adsorptive gas, the aperture and particle interval decline by embedment, swelling and

particle deformation with residual values of b_l and w_l , respectively. The changing of fracture porosity results in various types of permeability evolution in Fig. 5. Conversely, we quantitatively analyze the dominated mechanisms utilizing the permeabilities between and within groups, as well as samples, gases and cases.

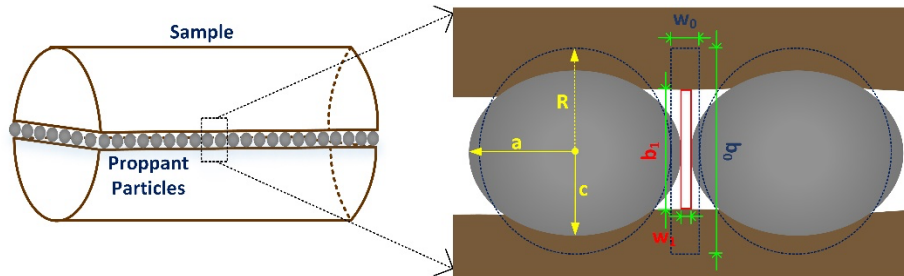


Fig. 6. Schematic of the evolution of fracture porosity in the shale.

4.1 Permeability dominated by effective aperture

Darcy's Law is applied to analyse the correlation between permeability and fracture porosity in the propped fracture. With the same confining pressure, gas pressure and gas property, the permeability ratio equals to the ratio of the flow rate, in other words, the flowing space that is roughly simplified into a rectangle space in Fig. 6. The permeability ratio is then calculated by

$$\frac{K_0}{K_1} = \frac{A_0}{A_1} = \frac{w_0 b_0}{w_1 b_1} \quad (3)$$

Where K_0 is the initial permeability; K_1 is the minished permeability; A , w and b are the interspace, particle interval and effective aperture, respectively. The subscripts have the same meanings as that in the K parameter.

In Eq. 3, the difference value of w is caused by the particle deformation and is minuscule for the high Young's Modulus (34.47 GPa) of the particle material. Besides, the deformation remains the same under the uniform effective pressure (confining pressure minus injection pressure), and the permeability ratio between groups is equal to the aperture ratio. The granite group is used as a reference, in which the aperture equals the particle diameter based on the first assumption. All data from shale groups has been processed and plotted in Fig. 7. The particle embedment depth approximately equals to half of the difference value between the initial particle diameter and the effective aperture, which varies from 0.05 to 0.15 mm. The same magnitude of embedment by morphological measurement has been reported in previous studies (Kumar et al., 2015; Li et al.,

2017), which fall into the range between 0.03 and 0.09 mm. The deviation is caused by the higher confining pressure in this study and the recovery of swelling when surface scanning was operated. A feature scaling has been performed for the obviousness on the permeability by converting its unit “m²” into “mD”. Four groups of similar scatter pattern have been discovered. In general, all points fall into a straight line. The CO₂ cases fit the line well, whilst the He cases follow the same line but gather into disarrayed clusters. The liquid CO₂ case also falls into the line. Yet, it overlaps into a point and no apparent rules can be observed. More details of this case will be discussed in 4.2.

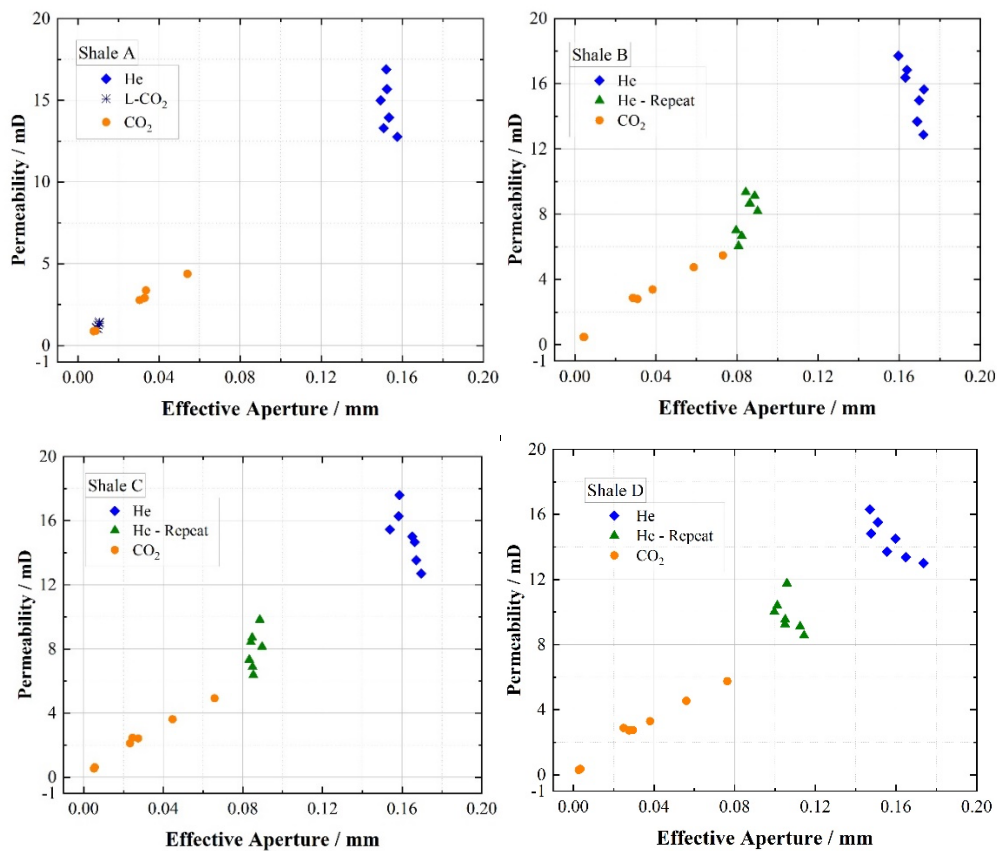


Fig. 7. Correlations between permeability and effective aperture in shale groups

A graphical explanation is shown in Fig. 8. The swelling effect expands the fracture surface and invades the aperture by the amount of Δb . Meanwhile, the soften rock matrix by CO₂ deepens the embedment depth. The remaining aperture (effective aperture) b_1 shrinks to a certain level and dominates the permeability evolution.

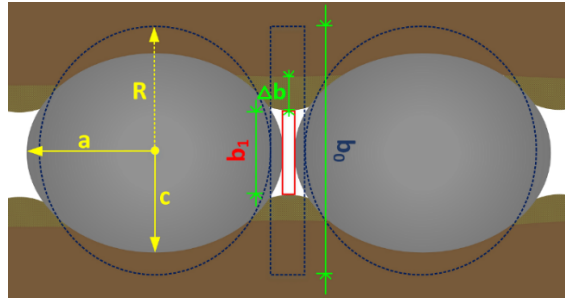


Fig. 8. Schematic of the evolution of fracture porosity in shale with injection of CO₂.

More details have been exhibited by integrating all data from He cases and CO₂ cases individually, as shown in Fig. 9. The CO₂ data points constitute a straight line no matter how various the permeability magnitudes are and what types of the evolution curve have formed (U or W-shaped). Noteworthy, the effective aperture also plays an important role among the He cases because all scatter fall to the same trend with CO₂ cases.

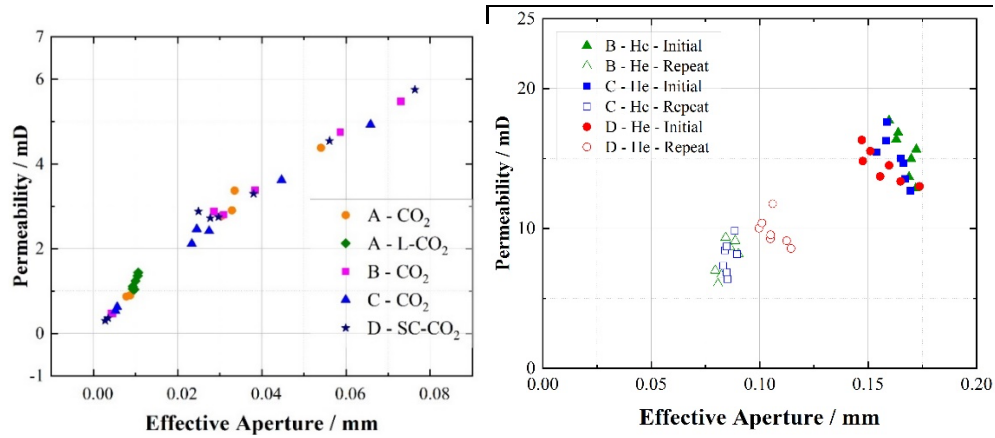


Fig. 9. Integrated results of permeability versus effective aperture with injections of CO₂ and He.

4.2 Permeability dominated by particle deformation

An indetectable but important phenomenon hides in He cases, which is the slightly upward skewing of the permeability value, as shown in Fig. 7. It indicates that some of the reduction factors have been omitted. The particle interval (w in Fig. 6) reduced by the deformation is under suspicion. To calculate the deformation, an elastic model is introduced referring to the nearby study (Kewen Li, 2015; White, Jordan, Spowart, & Thadhani, 2019).

$$\gamma = 1.04D(m^2 P_{eff} \frac{1-\nu^2}{E})^{2/3} \quad (4)$$

Where γ is the vertical deformation (“c” direction in Fig. 6) in radius; D is the particle diameter; m is the particle interval coefficient ($m=1$ when particles are uniformly displaced); P_{eff} is effective pressure

operating on the particle; ν and E are particle Poisson's Ratio and Young's Modulus. The parameter values and units are shown in Table 2.

Table 2. Calculation parameters and values.

D / mm	m	ν	E / GPa
0.2884	1	0.2	34.47

The minor axis c can be calculated by deformation γ that is μm level and is two orders of magnitude less than the aperture change in the sorbing case and one order of magnitude less than that in the non-sorbing case. Therefore, the first assumption is tenable.

The particle major axis a that invades the interspace width can be calculated by the volume conservation

$$a = \sqrt{\frac{D^3}{8(D/2 - \beta)}} \quad (5)$$

Different from the aperture analyses, there is no reference value of the initial particle interval. The particle major axis is then used for fitting the correlation within each He case. The parallel inverse linear relationships are observed in Fig. 10. The permeability gap between the initial and repeated cases is generated by the aperture difference induced by CO_2 . Fig. 11 has visually explained the decisive influence of particle deformation on permeability within the He case.

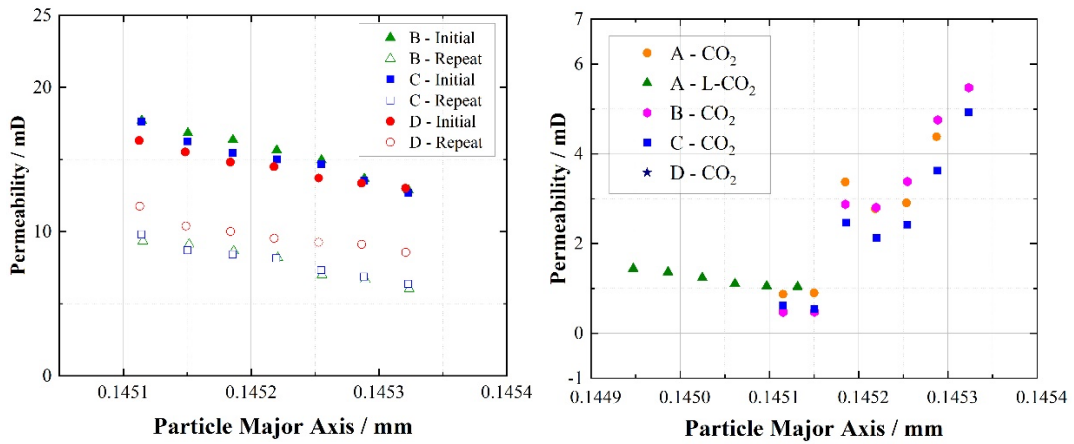


Fig. 10. Integrated results of permeability evolution versus deformation in the direction of the particle major axis with injections of CO_2 and He.

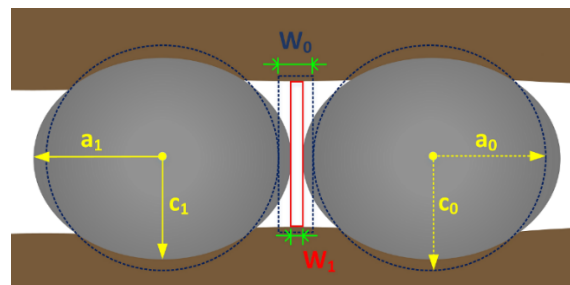


Fig. 11. Schematic of the evolution of fracture porosity in shale with injection of He.

There is an exception existing in liquid CO₂ case, whose results are presented in a double ordinate in Fig. 12. The permeability is both proportional to the effective aperture and inversely proportional to the particle major axis. Since the liquid CO₂ case shows the lowest permeability, the swelling and embedment are still dominative. Meanwhile, the injection pressure is much higher and counteracts half of the overburden on particles and rises the deformation effect up to a decisive level. Those dual functions result in a bi-linearity as shown in Fig. 12.

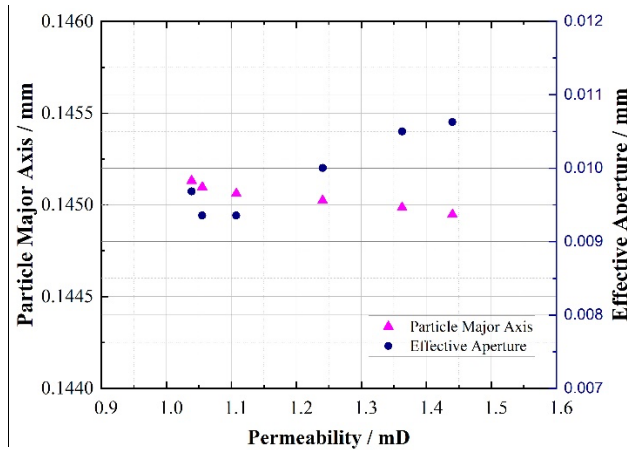


Fig. 12. The bi-linear evolution of permeability with the injection of liquid CO₂.

4.3 Embedment induced by swelling

We quantitatively distinguish the embedment and swelling by contrastive analyses. The aperture reduction ($\frac{b_0 - b_1}{2}$ as shown in Fig. 8) is calculated by Eq. 3. The swelling (Δb as shown in Fig. 8)

equals to the different value of aperture reduction between CO₂ and repeated He tests. Then, the adsorption ratio is calculated by the Langmuir isothermal adsorption equation, which is proposed as a key parameter for evaluating the embedment induced by swelling. The deformation of the Langmuir equation is as followed

$$\frac{V}{V_L} = \frac{P}{P_L + P} \quad (6)$$

Where the V is the adsorped amount; V_L is the Langmuir volume; P is the injection pressure; P_L is the Langmuir pressure and is 2.5 MPa under the experimental condition in this study.

Besides, the embedment in He case is calibrated considering the particle deformation. The deformation γ is calculated by Eq. 4 under each pressure condition and added to the averaged embedment of each case, as shown in Fig. 13. The gap between the initial and repeated value is

generated by the unrecoverable aggravation of embedment induced by swelling. The fluctuation of the original data is around 0.01 mm level and is one order of magnitude less than the embedment value in CO₂ case. We use this calibration instead of the mean value to improve the accuracy.

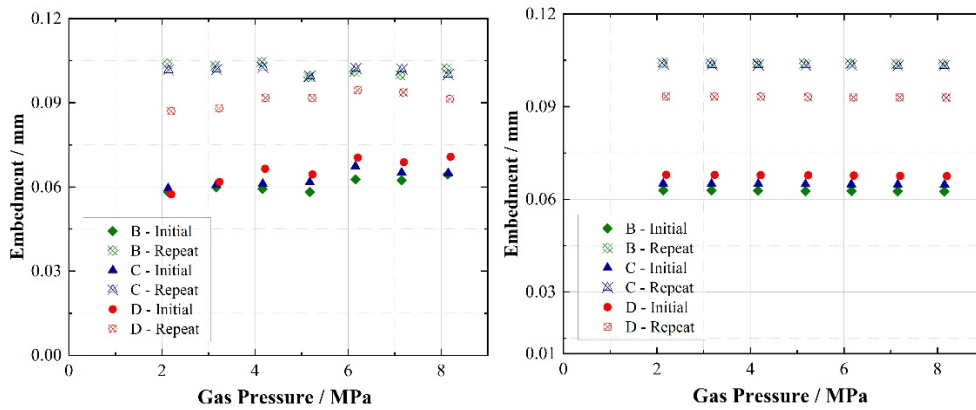


Fig. 13. Embedment relative to gas pressure for He. The left figure is the original data. The right one is the calibrated data.

The results have been plotted in Fig. 14. Generally speaking, both embedment and swelling are proportional to the adsorption ratio. The swelling contributes 5 to 35 % of the total aperture reduction, which already indicates a significant effect on permeability evolution individually.

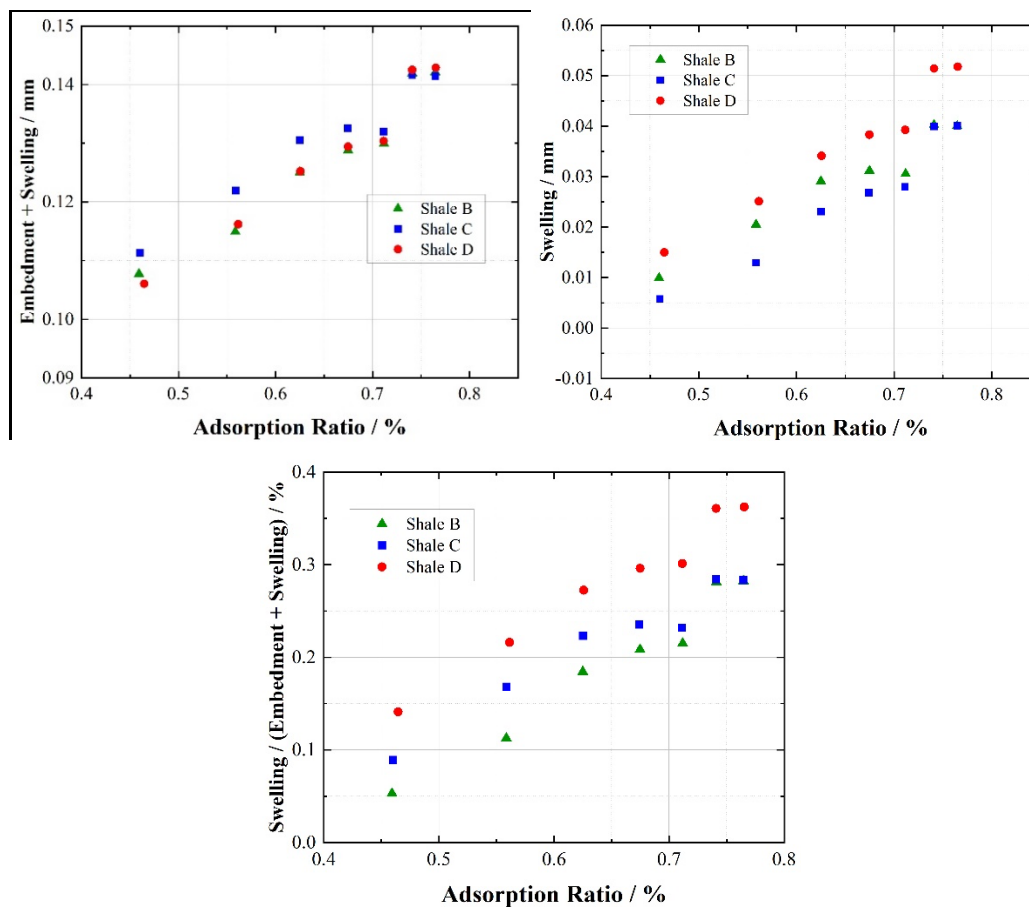


Fig. 14. Evolution of swelling and embedment relative to adsorption ratio for CO₂.

More common outcomes have been generated by fitting the relation between aperture reduction ratio and adsorption ratio, as shown in Fig. 15. The swelling aggravates the embedment by 1.3 to 1.7 times between the He cases. Regarding the sorbing gas case, the aperture reduction can be calibrated by fitting the empirical equation

$$\frac{AR_1}{AR_0} = 1.739 \frac{P}{P_L + P} + 0.845 \quad (7)$$

Where the AR_1 is the calibrated aperture reduction ($\frac{b_0 - b_1}{2}$ as shown in Fig. 8); AR_0 is the aperture reduction neglecting the swelling effect. The AR_1 takes the swelling effect into consideration and improves the prediction of the permeability in propped fractures. It is also helpful for the evaluation of CO₂ storage capacity, security and long-term migration.

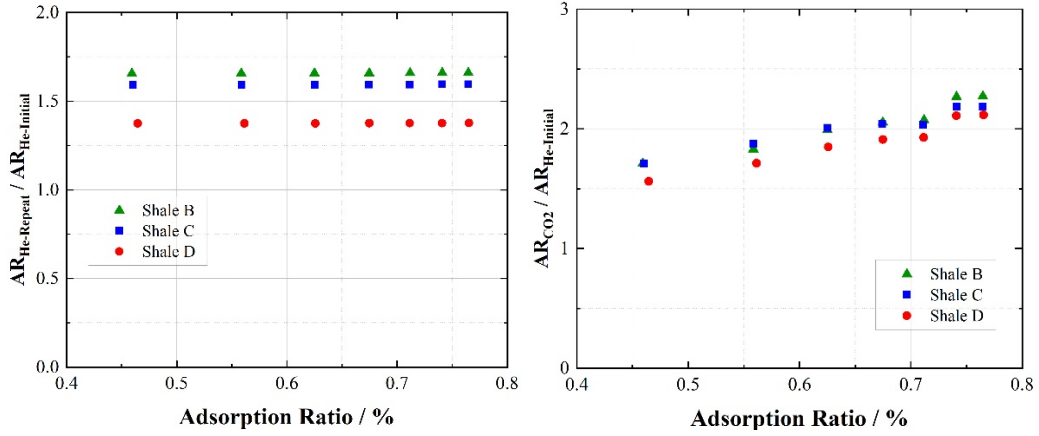


Fig. 15. Aperture reduction ratio versus adsorption ratio for various samples.

4.4 Verification

To test the universality of Eq. 7, an indirect method is proposed because of the shortage of direct real-time measurements of embedment and swelling. The permeability is the target parameter for the verification. The correlation between effective flowing interspace and permeability is simplified to a proportional relation and calculated by Eq. 8. Then, the non-sorbing gas permeability is applied to predict the permeability in the sorbing gas case. The procedure above is accomplished by the following equations

$$K = \alpha b_{eff} w = \alpha (D - 2AR) w \quad (8)$$

$$AR = (D - \frac{K}{\alpha w}) / 2 \quad (9)$$

$$\frac{AR_1}{AR_0} = \frac{\alpha w D - K_1}{\alpha w D - K_0} = 1.739 \frac{P}{P_L + P} + 0.845 \quad (10)$$

Where α is the slope of the interspace-permeability correlation and is obtained through trial and error method; b_{eff} is the effective aperture; w is the particle interval that is assigned to the value of the particle radius; D is the averaged particle diameter; K_i is the predicted permeability for sorbing gas case; K_0 is the measured permeability of non-sorbing case from the corresponding series of experiment.

Different types of sample and injection gas have been optimized from previous experiments (Kumar et al., 2015; Li et al., 2017), including coal sample (with an injection of CO_2) and CH_4 gas (in a propped shale sample). In the coal case, the 70 ~ 140 mesh proppant with an averaged diameter of 0.159 mm is used. The Langmuir pressure is closed to 1.75 MPa based on the minimum point on the permeability curve. The averaged diameter and Langmuir pressure are 0.288 mm and 3.5 MPa in the CH_4 case, respectively. The optimized slopes are 1.8×10^{-7} for CH_4 case and 7.8×10^{-7} for coal case when the units of permeability and flowing interspace are both “ m^2 ”. In this study, the slope is 6.5×10^{-7} and has the same magnitude. The results are plotted in Fig. 16. The gaps may be caused by the simplification of Eq. 8 and the randomly distributed particle interval. Nonetheless, the predictions fit the measurements well and similar trends are shown apparently.

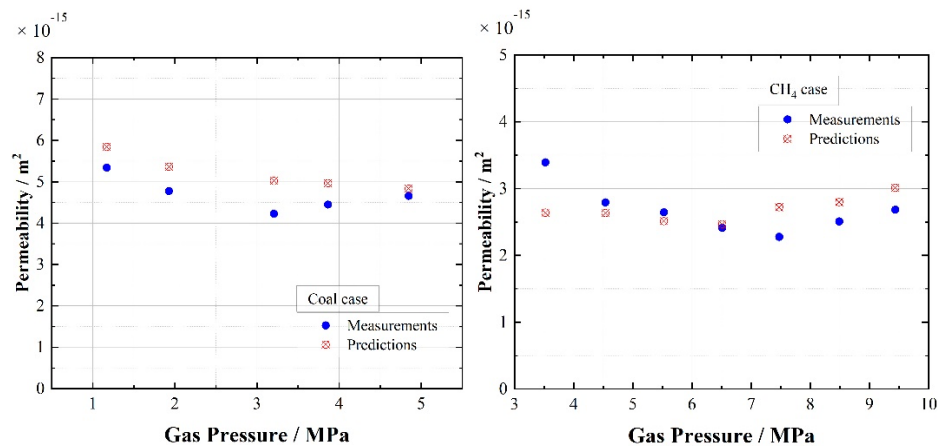


Fig. 16. Permeability prediction and comparison for coal and CH_4 .

5 Conclusions

Permeabilities of non-adsorptive He and adsorptive CO_2 in propped shale fracture have been tested alternatively. The effective aperture after embedment and swelling has been evaluated using the granite permeability as a reference. The particle interval variation has been calculated by its

deformation. Further analyses and regression have been carried out by introducing the Langmuir isotherm equation. The main outcomes are as followed:

(1) the linear relationship is found in permeability evolution curve for non-sorbing He cases, as well as the typical U-shaped curve for gaseous CO₂ cases and W-shaped curve for supercritical CO₂ case.

The parallel curves are discovered in the repeated He cases after the injection of CO₂. Approximately 50 ~ 70% of the permeability recovers by the recovery of swelling after the desorption of CO₂.

(2) a positive linear correlation between the effective aperture and the permeability is revealed by plotting all CO₂ cases in one coordinate despite the magnitudes of the value and curve types (U or W-shaped). The effective aperture dominates the permeability evolution in sorbing cases. The non-sorbing He cases distribute along the same straight line in disarrayed clusters and are slightly upward skewing.

(3) within the He case, the particle interval is demonstrated to dominate the permeability evolution. The deformation in particle major axis is calculated and fitted with the permeability. The negative linear parallel relations are discovered for all He cases.

(4) the liquid CO₂ case has the lowest permeability and a unique bi-linearity in the relations between permeability and effective aperture and particle major axis. The high injection pressure counteracts half of the overburden on particle and rises the deformation effect up to a similar dominating level as the swelling does.

(5) further analyses indicate that the swelling individually contributes 5 to 35 % of the aperture reduction (swelling plus embedment) according to the adsorped mass. It also aggravates the embedment by 1.3 to 1.7 times comparing the initial and repeated permeability in He cases in the same sample. A new calibration equation for aperture reduction is generated by bringing in the Langmuir isothermal equation and is verified by previous experiments on different rock type (coal) and with different sorbing gas (CH₄). It provides a more accurate method for the prediction of fracture conductivity that furtherly improves the gas recovery. It also benefits the understanding of CO₂ sealing behaviour and long-term migration, thus improves the evaluations of CO₂ storage capacity and security.

Acknowledgements



This research has received funding from the European Union's Horizon 2020 research and innovation programme under the Marie Skłodowska-Curie grant agreement No 846775.

References

- Alvarado, V., & Manrique, E. (2010). Enhanced Oil Recovery: An Update Review. *Energies*, 3(9), 1529-1575. doi:10.3390/en3091529
- Arshadi, M., Zolfaghari, A., Piri, M., Al-Muntasheri, G. A., & Sayed, M. (2017). The effect of deformation on two-phase flow through proppant-packed fractured shale samples: A micro-scale experimental investigation. *Advances in Water Resources*, 105, 108-131. doi:10.1016/j.advwatres.2017.04.022
- Bandara, K. M. A. S., Ranjith, P. G., & Rathnaweera, T. D. (2019). Improved understanding of proppant embedment behavior under reservoir conditions: A review study. *Powder Technology*, 352, 170-192. doi:10.1016/j.powtec.2019.04.033
- Bielicki, J. M., Langenfeld, J. K., Tao, Z., Middleton, R. S., Menefee, A. H., & Clarens, A. F. (2018). The geospatial and economic viability of CO₂ storage in hydrocarbon depleted fractured shale formations. *International Journal of Greenhouse Gas Control*, 75, 8-23. doi:10.1016/j.ijggc.2018.05.015
- Brace, W. F., Walsh, J. B., & Frangos, W. T. (1968). Permeability of granite under high pressure. *Journal of Geophysical Research*, 73(6), 2225-2236. doi:10.1029/JB073i006p02225
- Dong Chen, Z. Y., Zhejun Pan, Yingfang Zhou, Jialiang Zhang. (2017). A permeability model for the hydraulic fracture filled with proppant packs. *Journal of Petroleum Science and Engineering*.
- Fan, C., Elsworth, D., Li, S., Zhou, L., Yang, Z., & Song, Y. (2019). Thermo-hydro-mechanical-chemical couplings controlling CH₄ production and CO₂ sequestration in enhanced coalbed methane recovery. *Energy*, 173, 1054-1077. doi:10.1016/j.energy.2019.02.126
- Gale, J. F. W., Laubach, S. E., Olson, J. E., Eichhuble, P., & Fall, A. (2014). Natural Fractures in shale: A review and new observations. *AAPG Bulletin*, 98(11), 2165-2216. doi:10.1306/08121413151
- Goodman, A., Sanguinito, S., Tkach, M., Natesakhawat, S., Kutchko, B., Fazio, J., & Cvetic, P. (2019). Investigating the role of water on CO₂-Utica Shale interactions for carbon storage and shale gas extraction activities – Evidence for pore scale alterations. *Fuel*, 242, 744-755. doi:10.1016/j.fuel.2019.01.091
- Guo, J., Wang, J., Liu, Y., Chen, Z., & Zhu, H. (2017). Analytical analysis of fracture conductivity for sparse distribution of proppant packs. *Journal of Geophysics and Engineering*, 14(3), 599-610. doi:10.1088/1742-2140/aa6215
- Hoek, E., & Martin, C. D. (2014). Fracture initiation and propagation in intact rock – A review. *Journal of Rock Mechanics and Geotechnical Engineering*, 6(4), 287-300. doi:10.1016/j.jrmge.2014.06.001
- Kewen Li, Y. G., Youchang Lyu. (2015). New Mathematical Models for Calculating Proppant Embedment and Fracture Conductivity. *SPE Journal*, 20(03), 1-12.
- Kumar, H., Elsworth, D., Liu, J., Pone, D., & Mathews, J. P. (2015). Permeability evolution of propped artificial fractures in coal on injection of CO₂. *Journal of Petroleum Science and Engineering*, 133, 695-704. doi:10.1016/j.petrol.2015.07.008
- Li, X., Feng, Z., Han, G., Elsworth, D., Marone, C., Saffer, D., & Cheon, D.-S. (2017). Permeability Evolution of Propped Artificial Fractures in Green River Shale. *Rock Mechanics and Rock Engineering*, 50(6), 1473-1485. doi:10.1007/s00603-017-1186-2
- Liang, F., Sayed, M., Al-Muntasheri, G. A., Chang, F. F., & Li, L. (2016). A comprehensive review on proppant technologies. *Petroleum*, 2(1), 26-39. doi:10.1016/j.petlm.2015.11.001
- Liang, W., Zhao, Y., Wu, D., & Dusseault, M. B. (2011). Experiments on Methane Displacement by Carbon Dioxide in Large Coal Specimens. *Rock Mechanics and Rock Engineering*, 44(5), 579-589. doi:10.1007/s00603-011-0143-8
- Liu, H.-H., & Rutqvist, J. (2009). A New Coal-Permeability Model: Internal Swelling Stress and Fracture–Matrix Interaction. *Transport in Porous Media*, 82(1), 157-171. doi:10.1007/s11242-009-9442-x

- Liu, H., Wang, F., Zhang, J., Meng, S., & Duan, Y. (2014). Fracturing with carbon dioxide: Application status and development trend. *Petroleum Exploration and Development*, 41(4), 513-519. doi:10.1016/s1876-3804(14)60060-4
- Liu, S., Zhang, R., Karpyn, Z., Yoon, H., & Dewers, T. (2019). Investigation of Accessible Pore Structure Evolution under Pressurization and Adsorption for Coal and Shale Using Small-Angle Neutron Scattering. *Energy & Fuels*, 33(2), 837-847. doi:10.1021/acs.energyfuels.8b03672
- Mazumder, S., & Wolf, K. H. (2008). Differential swelling and permeability change of coal in response to CO₂ injection for ECBM. *International Journal of Coal Geology*, 74(2), 123-138. doi:10.1016/j.coal.2007.11.001
- Middleton, R. S., Carey, J. W., Currier, R. P., Hyman, J. D., Kang, Q., Karra, S., . . . Viswanathan, H. S. (2015). Shale gas and non-aqueous fracturing fluids: Opportunities and challenges for supercritical CO₂. *Applied Energy*, 147, 500-509. doi:10.1016/j.apenergy.2015.03.023
- Pan, Z., & Connell, L. D. (2011). Modelling of anisotropic coal swelling and its impact on permeability behaviour for primary and enhanced coalbed methane recovery. *International Journal of Coal Geology*, 85(3-4), 257-267. doi:10.1016/j.coal.2010.12.003
- Pini, R., Ottiger, S., Burlini, L., Storti, G., & Mazzotti, M. (2009). Role of adsorption and swelling on the dynamics of gas injection in coal. *Journal of Geophysical Research*, 114(B4). doi:10.1029/2008jb005961
- Rani, S., Padmanabhan, E., & Prusty, B. K. (2019). Review of gas adsorption in shales for enhanced methane recovery and CO₂ storage. *Journal of Petroleum Science and Engineering*, 175, 634-643. doi:10.1016/j.petrol.2018.12.081
- Santos, L., Dahi Taleghani, A., & Li, G. (2018). Expandable proppants to moderate production drop in hydraulically fractured wells. *Journal of Natural Gas Science and Engineering*, 55, 182-190. doi:10.1016/j.jngse.2018.04.026
- Tang, Y., & Ranjith, P. G. (2018). An experimental and analytical study of the effects of shear displacement, fluid type, joint roughness, shear strength, friction angle and dilation angle on proppant embedment development in tight gas sandstone reservoirs. *International Journal of Rock Mechanics and Mining Sciences*, 107, 94-109. doi:10.1016/j.ijrmms.2018.03.008
- Wang, J., & Elsworth, D. (2018). Role of proppant distribution on the evolution of hydraulic fracture conductivity. *Journal of Petroleum Science and Engineering*, 166, 249-262. doi:10.1016/j.petrol.2018.03.040
- Wang, S., Elsworth, D., & Liu, J. (2011). Permeability evolution in fractured coal: The roles of fracture geometry and water-content. *International Journal of Coal Geology*, 87(1), 13-25. doi:10.1016/j.coal.2011.04.009
- Wang, S., Elsworth, D., & Liu, J. (2013). Permeability evolution during progressive deformation of intact coal and implications for instability in underground coal seams. *International Journal of Rock Mechanics and Mining Sciences*, 58, 34-45. doi:10.1016/j.ijrmms.2012.09.005
- Wen, Q., Zhang, S., Wang, L., Liu, Y., & Li, X. (2007). The effect of proppant embedment upon the long-term conductivity of fractures. *Journal of Petroleum Science and Engineering*, 55(3-4), 221-227. doi:10.1016/j.petrol.2006.08.010
- Weng, X. (2015). Modeling of complex hydraulic fractures in naturally fractured formation. *Journal of Unconventional Oil and Gas Resources*, 9, 114-135. doi:10.1016/j.juogr.2014.07.001
- White, B. W., Jordan, J. L., Spowart, J. E., & Thadhani, N. N. (2019). Particle Strain Analysis of Epoxy-Based Composites Following Quasi-Static and Dynamic Compression. *Journal of Dynamic Behavior of Materials*, 5(1), 24-38. doi:10.1007/s40870-019-00182-2
- Zhang, J., & Hou, J. (2016). Theoretical conductivity analysis of surface modification agent treated proppant II – Channel fracturing application. *Fuel*, 165, 28-32. doi:10.1016/j.fuel.2015.10.026
- Zhang, J., Ouyang, L., Zhu, D., & Hill, A. D. (2015). Experimental and numerical studies of reduced fracture conductivity due to proppant embedment in the shale reservoir. *Journal of Petroleum Science and Engineering*, 130, 37-45. doi:10.1016/j.petrol.2015.04.004

- Zhang, T., Yang, S., Jiang, X., & Dong, S. (2016). Sub-Seasonal Prediction of the Maritime Continent Rainfall of Wet-Dry Transitional Seasons in the NCEP Climate Forecast Version 2. *Atmosphere*, 7(2). doi:10.3390/atmos7020028
- Zhang, X., Lu, Y., Tang, J., Zhou, Z., & Liao, Y. (2017). Experimental study on fracture initiation and propagation in shale using supercritical carbon dioxide fracturing. *Fuel*, 190, 370-378. doi:10.1016/j.fuel.2016.10.120
- Zhi, S., Elsworth, D., & Liu, L. (2019). W-shaped permeability evolution of coal with supercritical CO₂ phase transition. *International Journal of Coal Geology*, 211. doi:10.1016/j.coal.2019.103221